RSC Advances

PAPER

View Article Online
View Journal | View Issue

Cite this: *RSC Adv.*, 2022, **12**, 36150

Reversible colorimetric sensing of volatile analytes by wicking in close proximity to a photonic film†

Timothy J. Palinski, ‡§[a] Bin Guan, §[bc] Bronwyn H. Bradshaw-Hajek, [c] Michael A. Lienhard,[a] Craig Priest *[bcd] and Félix A. Miranda[a]

Isolation of volatile analytes from environmental or biological fluids is a rate-determining step that can delay the response time for continuous sensing. In this paper, we demonstrate a colorimetric sensing system that enables the rapid detection of gas-phase analytes released from a flowing micro-volume fluid sample. The sensor platform is an analyte-responsive metal-insulator-metal (MIM) thin-film structure integrated with a large area quartz micropillar array. This allows precise planar alignment and microscale separation (310 μm) of the optical and fluidic structures. This configuration offers rapid and homogeneous color changes over large areas that permits detection by low-resolution optics or eye, which is well-suited to portable/wearable devices. For our proof-of-principle demonstration, we utilized a poly(methyl methacrylate) (PMMA) spacer and evaluated the sensor's response (color change) to ethanol vapor. We show that the RGB color value is quantitatively linked to the spacer swelling, which is reversible and repeatable. The optofluidic platform reduces the sensor response time from minutes to seconds compared with experiments using a conventional chamber. The sensor's concentration-dependent response was examined, confirming the potential of the reported sensing platform for continuous, compact, and quantitative colorimetric analysis of volatile analytes in low-volume samples, such as biofluids.

Received 25th October 2022
Accepted 17th November 2022

DOI: 10.1039/d2ra06740d

rsc.li/rsc-advances

Introduction

Small, simple, accurate, and real-time biochemical sensors are needed for numerous applications ranging from point-of-care medical diagnostics to food quality monitoring.[1–6] These sensors especially have the potential to enable completely new diagnostic capabilities in resource-limited scenarios, where larger, lab-based sensing systems are impractical. One such application is astronaut health monitoring, where accurate, real-time device operation in a compact platform is critically needed.[7] Sensor robustness, repeatability, and continuous monitoring of key diagnostic indicators are also highly desired.[7] Wearable sensors based on microfluidics offer a promising approach to these challenges.[8,9] Microfluidic techniques are able to confine and control micro/nanoliters of fluid at small scales, providing opportunities for autonomous sample collection and delivery.

Volatile analytes are present in biofluids and are being investigated to offer new avenues for non-invasive health monitoring.[10–13] Volatile organic compounds (VOCs) can be employed as biomarkers for various diseases or disorders.[14–16] For example, VOCs in breath can be associated with radiation exposure,[17,18] which is a significant concern for astronauts in outer space. Moreover, vapor detection from fluid samples (*e.g.*, sweat and saliva) can achieve real-time continuous monitoring and provide insights into one's health status. However, the detection of vapor analytes is often delayed by the slow diffusion-limited transmission of analytes from the liquid phase through the ambient vapor phase to the sensor. To improve analyte transport and enable rapid vapor detection with microfluidic techniques in wearable devices is hence the focus of this paper.

Multiple sensing mechanisms have been utilized in wearable devices, including electrochemical, optical, and piezoelectric, among others.[12] Optofluidic devices, which combine the advantages of precise fluid manipulation (microfluidics) with the speed and sensitivity of optical sensing, are receiving a lot of attention.[19–21] Nonetheless, optofluidic devices often lack portability due to extensive off-chip hardware. One approach to low-cost, portable optofluidic sensing is to induce a color change that can be easily observed by users without complicated equipment for signal readout. For example, in photonic

[a]*Communications & Intelligent Systems Division, NASA Glenn Research Center, Cleveland, Ohio 44135, USA*

[b]*Future Industries Institute, University of South Australia, Mawson Lakes, SA 5095, Australia*

[c]*UniSA STEM, University of South Australia, Mawson Lakes, SA 5095, Australia. E-mail: craig.priest@unisa.edu.au*

[d]*Australian National Fabrication Facility – South Australia Node, University of South Australia, SA 5095, Australia*

† Electronic supplementary information (ESI) available. See DOI: https://doi.org/10.1039/d2ra06740d

‡ Current address: Honeywell International, Inc. Broomfield, CO. USA.

§ The authors contributed equally to this work.

nanomaterial-based colorimetric sensors, the change of color is caused by a change in local refractive index and/or structural change in the presence of analytes, which is referred to as "structure colors".[22–24] Compared to other colorimetric sensors (*i.e.*, reagent-based sensors), structural color sensors are especially adaptable for wearable sensing because they are reversible (*i.e.*, return to the normal state after removal from the presence of the analyte), they do not require chemical reagents, and they are suitable for use in remote environments, such as in space, enabling continuous and real-time operation.

Herein, we report an optofluidic sensing platform (Fig. 1) for rapid detection of vapor from liquid samples based on structural color change. The platform is composed of both an optical sensing component and a microfluidic element. The optical sensing component is based on a previously reported nanoisland metal-insulator-metal (MIM) cavity structure.[25] Unlike a typical continuous-film MIM cavity, which produces a narrowband reflectance dip at the Fabry–Perot (FP) resonance condition resulting in comparatively dull band-stop reflective colors, this nanoisland MIM structure produces a well-defined reflectance peak at the FP resonance condition, owing to strong off-resonance absorption by the plasmonic nanoisland top film.[25–27] This results in brighter, more vibrant reflective colors, which depend critically upon the spacer thickness. By incorporating a polymer spacer that swells in the presence of the analytes of interest, a reversible, tunable colorimetric response is achieved.[25,28,29]

The microfluidic element accelerates the sensor response to the changing analyte concentration in the vapor phase by minimizing the length-scale between the sample (a solution containing the volatile analyte) and the sensing material, using a capillary-driven wicking phenomenon. The capillary wicking is enabled by an array of micropillars with well-designed dimensions and lattice spacing.[30] This open micropillar array can effectively sustain an evaporation-driven flow for sample delivery, that is, the loss of fluids by evaporation from the array is continuously compensated by the introduction of fluid from a reservoir. As reported previously,[31,32] the liquid transport dynamic on the pillar array is insensitive to varied sample and ambient conditions, and hence it will be suitable for use in challenging environments, such as microgravity.

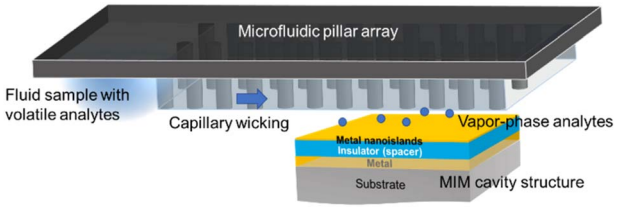

Fig. 1 The optofluidic sensing platform for the rapid detection of vapor analytes from fluid samples.

Experimental

Sensor fabrication

The thin-film MIM sensor was fabricated on a 45 nm Gold (Au)-coated silicon substrate. Poly(methyl methacrylate) (PMMA) thin film was prepared by spin coating 10% (w/v) PMMA (Mw ~120 000 by GPC, Sigma-Aldrich) that was dissolved in anisole (ReagentPlus®, 99%, Sigma-Aldrich) on the Au-coated substrate at various speeds ranging from 500 rpm to 3500 rpm for 1 min, followed by baking on a hot plate at 180 °C for 1 min. The top Au nanoislands were formed by magnetron sputtering (HHV TF500) on the PMMA-coated substrate at a rate of 0.36 nm s^{-1} for 3 s. Simulations of the optical stack (described later) are consistent with a 3 nm thick effective medium layer (mixture of air and gold). The PMMA thin film thickness was measured using a spectroscopic ellipsometer (J. A. Woollam, MC-200) at three incidence angles of 65°, 70° and 75°. The wavelength was varied between 250 and 800 nm by a step of 10 nm. The acquired data was modelled using the Cauchy approximation in the WVASE 32 software to extract the thickness value.

The micropillar arrays were prepared in fused silica by UV photolithography and plasma etching. A 6 in. diameter fused silica (quartz) wafer was first sputter coated with 100 nm of chromium (Cr) (HHV TF500) as an anti-reflection layer, and then spin coated with a layer of SU8-10 photoresist. After pre-baking, the photoresist layer on the quartz wafer was exposed to UV (360 nm) through a Cr-glass photomask of circular patterns (EVG 620), followed by post-baking and development by using propylene glycol monomethyl ether acetate. Plasma etching (ULVAC, NLD570) with argon and octafluoropropane (C_3F_8) gases was carried out to sequentially remove the exposed Cr and then etch the silica to the required depth. The remaining Cr on the top of each pillar was etched away by 10% (w/v) ceric ammonium nitrate solution to give a totally transparent micropillar chip. The pillars are 10 μm diameter and 20 μm height, arranged with a 20 μm square lattice spacing. Scanning electron microscopy (SEM, Zeiss Crossbeam 540) was used to image the micropillar array.

Optical characterization

Light from a halogen light source (HL-2000, Ocean Optics) was focused onto the MIM sample surface at zero incident angle *via* a bifurcated optic fiber. The reflectance spectra were collected using a fiber-coupled spectrometer (Ocean Optics QE Pro). All measurements were referenced to an $R > 97.5\%$ reflective silver (Ag) mirror and normalized according to eqn (1):

$$S(\lambda) = \frac{R_S(\lambda) - N(\lambda)}{R_{ref}(\lambda) - N(\lambda)} \quad (1)$$

where $S(\lambda)$ is the normalized sensor output, R_S is the raw spectrum reflected from the sample, R_{ref} is the reflected spectrum from the Ag reference mirror, and N is the noise spectrum (dark signal) obtained by blocking all light incident on the spectrometer entrance slit.

Vapor sensing experiments

The vapor sensing experiments were conducted at room temperature (23 °C). For bulk testing, the samples were placed in three closed chambers with approximate gas volumes of 70 mL, 28 mL and 8.5 mL. A reservoir of solvent was added in to

provide the vapor source and the solvent volume was in excess to ensure vapor saturation within the chamber. The area of solvent/air interface where the solvent evaporation happens was set to be proportional to the volume of the chamber which the vapor need to fill. The trapped vapor is assumed to quickly reach saturation:[33] $P_{sat} \approx 5\% P_{atm}$. P_{sat} and P_{atm} refer to saturation pressure and atmospheric pressure, respectively.

The microfluidic sensing tests were conducted as follows: a micropillar chip was placed upside down on a chip holder to ensure its pillar array region is suspended over the sample at a fixed distance of 310 μm. This distance was decided based on instrumental limitation. A small volume (μL) of solvent was loaded to the edge of the chip, which quickly (1–2 s) fills the pillar array *via* wicking.[32] The thin liquid film formed in the pillar array enables efficient evaporation of the dissolved solvent (analyte) and can quickly equilibrate the vapor in the microenvironment between the chip and the sample. The volume of this semi-confined microenvironment (referred as an "open-wall" chamber) was calculated to be 18.6 μL or 310 nL mm^{-2}.

The reflected color change of the MIM surface upon volatile sample exposure was tracked by an epi-illumination microscope (Motic BA 210) with a 20× objective and a CMOS camera (Moticam 2500) for further color analysis. The optical reflectance spectra of the sensor were also monitored and recorded every 1 s over the exposure time. To reduce the optical interference from the pillar array on the top of the sensor, a pillar-free window (approximately 0.5 × 0.5 mm) was created by physically removing some pillars for the spectra collection and image capture.

Simulations

The optical response of the thin-film structures was simulated using the transfer matrix method (TMM), based on freely available MATLAB code.[34] The multi-layer stack was modeled with layer thicknesses t_n and refractive indexes n_n as follows: air ($t_1 = \infty$, $n_1 = 1.0$); Au nanoisland film ($t_2 = 3$ nm, $n_2 =$ measured complex refractive index[25]); PMMA spacer ($t_3 =$ 300–600 nm, $n_3 = 1.49$); Au mirror ($t_4 = 45$ nm, $n_4 =$ optical constants for gold from Johnson & Christy data[35]); Si wafer ($t_5 = \infty$, $n_5 = 3.8$). Light was normally-incident from above (through the air region), and the reflectance, transmittance, and absorbance coefficients were calculated for the structure.

Results and discussion

Principle of operation

In this proof-of-principle demonstration, we used (PMMA) as the spacer material in the MIM sensor, as it is readily available and responds to a range of organic vapors including ethanol, methanol, acetone, and isopropanol.[36] Ethanol was chosen as a volatile model analyte to demonstrate the sensing configuration, as it is a typical volatile compound with implications to diseases such as non-alcoholic steatohepatitis and obesity. Note that the selective detection of multiple organic vapors may be possible through choosing the appropriate polymer spacer.[37–40]

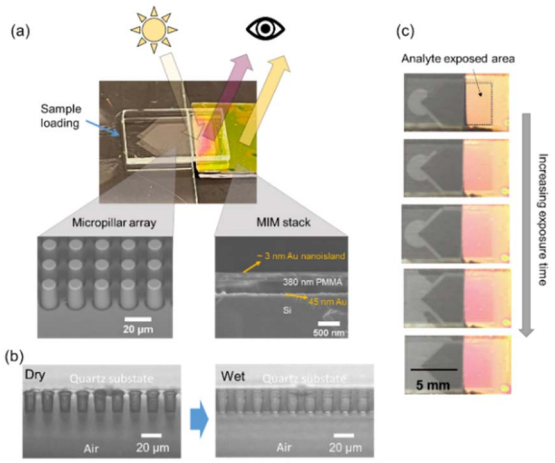

Fig. 2 Sensor overview and operating principle. (a) The optofluidic sensor consists of a MIM thin-film stack and a quartz micropillar chip in close proximity to the thin film surface. The gap between the chip and the sensor is 310 μm. Scanning electron micrographs reveals the MIM structure: 3 nm Au nanoislands/$d \approx$ 380 nm responsive polymer/45 nm Au mirror on a silicon substrate, and the pillars of 10 μm diameter and 20 μm height, arranged with a 20 μm square lattice spacing. When white light illuminates the MIM structure from above, it shows a bright reflected color and the color is determined primarily by polymer thickness. (b) Profiles of the quartz micropillar array before and after fluid sample loading. A well-defined liquid film is formed on the array. (c) Volatile analytes delivered *via* the micropillar chip to the sensor cause polymer swelling and reflected color change over time.

Alternatively, an array of the MIM sensors with varying spacers, coupled with chemometric analysis could achieve multiplexed detection.[41,42] However, this is beyond the scope of the current study.

The colorimetric optofluidic sensor integrates a thin-film MIM stack: 3 nm Au nanoisland/~380 nm PMMA/45 nm Au mirror on a silicon (Si) wafer, and a quartz micropillar array for effective analyte delivery (Fig. 2a). When exposed to the analyte, the PMMA layer in the MIM stack swells, producing a different reflected color (magenta) from its original color (gold) (Fig. 2a). The micropillar array, in its current dimensions, facilitates spontaneous liquid filling into void spaces between pillars *via* capillarity, *i.e.*, wicking (Fig. 2b). When a liquid thin film evaporates from the array, additional liquid from the reservoir will be drawn to refill and thus create a continuous flow in the array area. In the sensing configuration, the array region faces directly to the sensor surface, which can create a confined local exposure on the sensor. A color change in the analyte exposed area develops over time as seen in Fig. 2c, corresponding to the change of the polymer thickness in the MIM stack due to analyte exposure.

Optical characterization

As a step towards a simplified, spectrometer-free sensing device, we analyzed the reflected colors of discrete calibration samples made with spacer thicknesses from 320 nm to 560 nm, several of which are shown in Fig. 3a. Their corresponding reflectance spectra were also recorded to correlate the reflectance peak

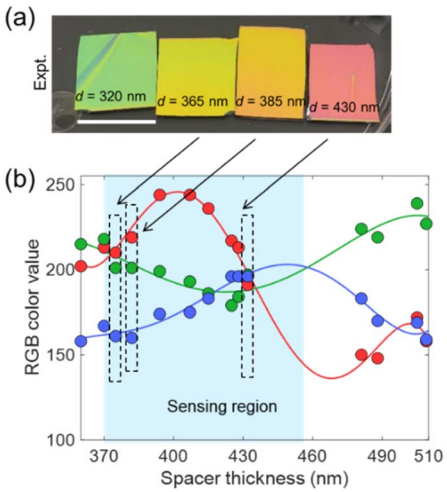

Fig. 3 Nanoisland MIM sensor design and color characterization. (a) Color photographs of several calibration samples with varied spacer thicknesses d. Scale bar 1 cm. (b) RGB calibration points derived from camera images at each spacer thickness (circle markers) and interpolated RGB calibration curves (continuous lines) using a 5th order polynomial fit. Spacer thicknesses were determined using ellipsometry. The approximate sensing region for spacer thicknesses studied in this work is shaded in blue.

wavelength with the spacer thickness (Fig. S1 in ESI†). Optical simulation results in Fig. S1c† demonstrate good agreement with experiments and provide guidance for the design and color space coverage of the sensors.

A calibration model was built from the color and spacer thickness data (Fig. 3b) and may therefore be used to convert the RGB value from the sensor color to an analyte-induced change in spacer thickness. This model relates the measured average RGB value (circle markers) for each calibration sample to a known spacer thickness d (measured by spectroscopic ellipsometry). The continuous curves represent a 5th order polynomial fit through each color set R, G, and B as a function of d.

Fig. 4 shows the workflow of color conversion. First, samples S1–S5 having unknown spacer thickness are imaged using a standard CMOS camera (*e.g.*, using a cell phone) and the average RGB color for each sample is calculated (Fig. 4a). Next, in Fig. 4b, each sample RGB triple RGB_S is compared to the RGB triples RGB_C in the calibration database developed in Fig. 3b. The minimum Euclidean distance between RGB_S and RGB_C is calculated for each spacer thickness d in the calibration set C, resulting in the estimated spacer thickness d_{est}:

$$d_{est} = \min_{d \in D} \sqrt{(r_s(d) - r_c(d))^2 + (g_s(d) - g_c(d))^2 + (b_s(d) - b_c(d))^2} \quad (2)$$

where r_S, g_S and, b_S comprise the sample RGB triple RGB_S; similarly for the calibration RGB triple RGB_C. Other metrics, including cosine similarity and other Minkowsky metrics (of which Euclidean distance is a special case) have also been applied to RGB analysis.[43] We chose Euclidean distance because of its success in previous studies,[5] as well as with our own data

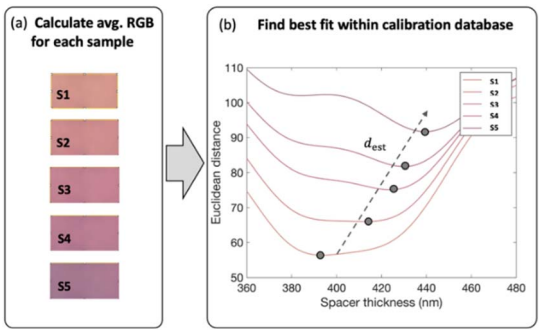

Fig. 4 Workflow for converting measured RGB color to estimated spacer thickness: (a) calculate average RGB vector (RGB_S) for each sample (S1–S5) from camera images. (b) For each spacer thickness d in the calibration dataset C, find the best fit between the sample vector RGB_S and the calibration vector RGB_C using a suitable distance metric (Euclidean distance here) to obtain the estimated spacer thickness d_{est}.

set. Finally, it is important to note that the images in the calibration database must be taken under the same controlled conditions as the test samples. This requirement is relatively easy to meet, *e.g.*, using a cell phone, given the repeatable reference illumination of the camera flash and built-in default image processing.

Therefore, using the workflow in Fig. 4, the RGB color images of the MIM structure captured by a camera reveal quantitative information about the corresponding polymer thickness. The RGB conversion process and fitting method are detailed further in the MATLAB code in the ESI.†

Micropillar array and sensing performance

To demonstrate the role of the micropillar array in this sensing system, we used 100% ethanol as a model analyte and exposed the nanoisland MIM sensor to ethanol vapor in two ways, *via* the micropillar array and *via* a conventional gas sensing chamber (hereafter referred as "bulk") (Fig. 5a). Three different sizes of conventional chambers were used to investigate the size effect on the sensing results. The reflectance peaks of the sensor were monitored by a spectrometer as a standard signal readout for optical sensing. The peak wavelength was converted to a polymer thickness value based on the calibration in Fig. S1 in the ESI.† The change in polymer thickness was then plotted against the analyte exposure time and the trend was compared between the pillar array and the bulk scenarios. Additionally, to verify the aforementioned RGB conversion, the RGB color change of the sensor in the pillar array scenario was also monitored to reveal the change in the polymer thickness as a function of time.

As shown in Fig. 5b, the polymer layer swells quickly when exposed to ethanol vapor and saturates after long-time exposure. Micropillar array-assisted sensing shows much quicker swelling, and the swelling process is reversible (Fig. S2 in ESI†). In the inset graph where only the response of the first 90 s is plotted, the ethanol vapor induces a substantial sensor response within 20 s, whereas it requires a minute or more for the bulk method. It is considered that a microscale virtual

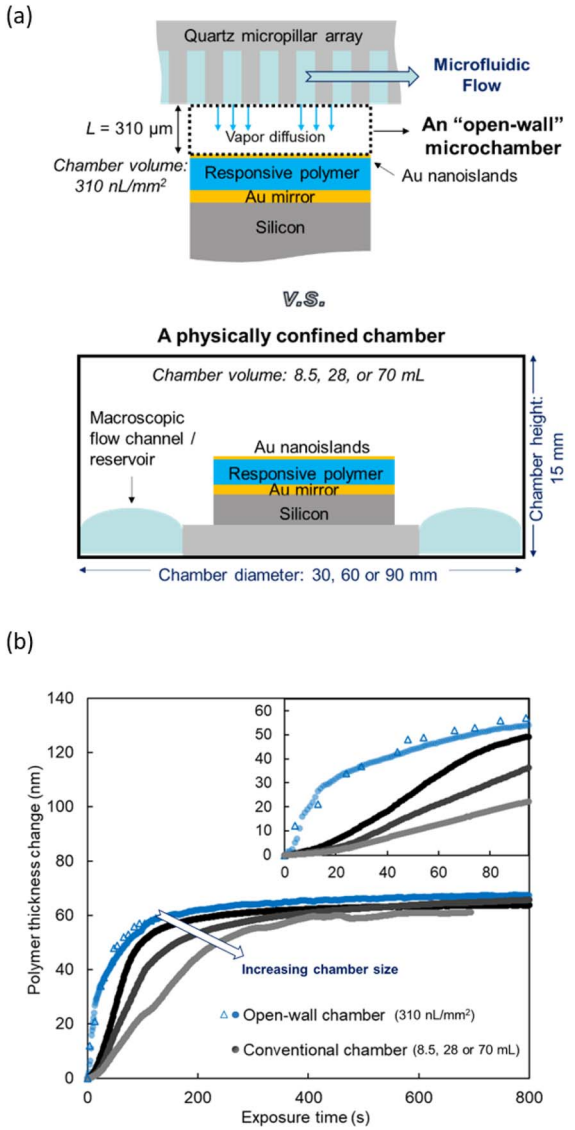

Fig. 5 Improved analyte delivery and sensing response using the microfluidic chip. (a) Two sensing configurations: an "open-wall" chamber enabled by the micropillar array *versus* a conventional gas sensing chamber with varying volume. (b) Corresponding sensor response is characterized by the spacer thickness change as a function of time. The spacer thickness in dot points was calculated based on the spectrometer-measured primary reflectance peak wavelength. The spacer thickness in triangle markers was estimated based on the sensor color, showing good agreement. The arrow indicates different sensor responses for the conventional chamber with increasing size. The inset graph shows the sensing response within the first 90 s of exposure for both configurations.

chamber is created between the microfluidic chip and the sensor surface in the pillar array scenario. The small chamber size reduces the time to reach an equilibrium of ethanol vapor near the sensor surface. This is also in agreement with the bulk results where the sensor response slows with increasing chamber size.

Moreover, the data in triangle markers in Fig. 5b derived from the RGB color change is consistent with that from the spectroscopic measurement, indicating the feasibility of the RGB color conversion for a spectrometer-free sensing strategy with our sensing platform.

In the micropillar array scenario, a mathematical model can be used to describe the diffusion of ethanol vapor into the polymer layer. Since the distance between the pillar array and polymer surface is only 310 μm, and the ethanol in the reservoir is continually replenished, we assume that the concentration of the ethanol vapor in the semi-confined space is constant. We also assume that there is an infinitesimally thin layer of "condensed" ethanol on the surface of the polymer. The concentration of ethanol in the polymer, $c(x,t)$, can then be described using the diffusion equation,

$$\frac{\partial c}{\partial t} = D\frac{\partial^2 c}{\partial x^2} \tag{3}$$

where x is the distance into the polymer, D is the diffusivity of ethanol in the polymer, and t is the time since the beginning of exposure. The constant concentration at the surface of the polymer is represented by $c(0,t) = c_0$ where c_0 is the concentration of ethanol in the thin layer, while we use a zero flux condition at the bottom of the polymer layer. This model can be solved using standard techniques, and the mass of ethanol that has been absorbed by the polymer can be calculated by simple integration over the thickness of the polymer. That is, the mass, $m(t)$, is given by

$$m(t) = A\times h\times c_0\left(1 - \frac{8}{\pi^2}\sum_{n=1}^{\infty}\frac{1}{(2n-1)^2}\exp\left(-\frac{D(2n-1)^2\pi^2 t}{4h^2}\right)\right) \tag{4}$$

where A is the surface area of the polymer exposed to the ethanol (*i.e.*, the area not covered by the Au nanoislands), and h is the thickness of the polymer (as a first approximation we ignore the fact that the polymer/ethanol combination may not mimic an ideal solution). The increase in mass can be converted to an increase in volume and subsequently an increase in thickness. Since the diffusivity of ethanol in the polymer is unknown, as is the surface area exposed to the ethanol, we can use both quantities as fitting parameters and fit eqn (4) to the experimental data obtained using the microfluidic sensor. A similar technique was used by Hou and Baltus.[44]

Fig. 6 shows the modelling and experimental results of polymer swelling of 100% ethanol exposure. Overall, the modelling curve shows a reasonably good agreement with the experimental one. The model predicts that the diffusivity of ethanol in the PMMA is 9.7×10^{-13} m^2 s^{-1} and that the Au nanoislands cover approximately 78% of the PMMA surface. The ethanol diffusivity in PMMA is consistent with the value found in the literature.[45] The predicted nanoisland coverage is also similar to the experimental value derived from the SEM image in Fig. S3 in ESI,† which is 73%. The model describes the diffusion of ethanol from the surface of the polymer into the polymer bulk. We observe good agreement between the model and experiment, which implies that diffusion in the polymer (rather than in the vapor) governs the time scale for the open-wall microchamber scenario.

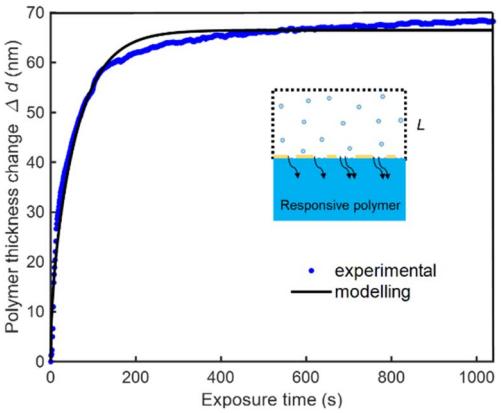

Fig. 6 Modelling of the ethanol vapor-induced polymer swelling over time in the "open-wall" chamber. In the sensing scenario, this virtual chamber is spontaneously formed between the micropillar array and the MIM sensor aiding the diffusion of ethanol vapor to the sensor. The model assumes a constant ethanol vapor concentration in the virtual chamber during the process and considers a constant-source diffusion of ethanol into the polymer. The experimental polymer thickness was calculated from the measured reflectance peak wavelength.

Spectrometer-free sensor readout

The sensor response to different concentrations of ethanol was evaluated by continuously tracking the color change of the sensor with an optical microscope. Fig. 7a shows the images of the sensor surface before and after 80 s of exposure to various concentrations of ethanol. It qualitatively shows a more distinct color change with higher ethanol concentration. Quantitatively, as described in Fig. 4, the RGB values of the images were calculated and fitted into the spacer thickness calibration model (Fig. 3b) to obtain the corresponding spacer thickness under different ethanol exposure times (Fig. S4 in the ESI†). Fig. 7b displays the change of spacer thickness as the function of the concentration of ethanol at 80 s of exposure. The RGB-derived thickness change in general agrees with the spectrometer measured data. The linearity (R^2 = 0.977) in the plot suggests analyzing the color change of the sensor is a promising route for quantitative detection of ethanol. It thus can be concluded that the MIM sensors studied here can be used as colorimetric sensors for easy spectrometer-free readout. It is worth noting that the sensitivity of this platform to analytes is primarily associated with the polymer spacer. By carefully choosing the optimal polymer spacer in the MIM stack, a range of other volatile analytes can be detected and both detection selectivity and sensitivity can be enhanced.

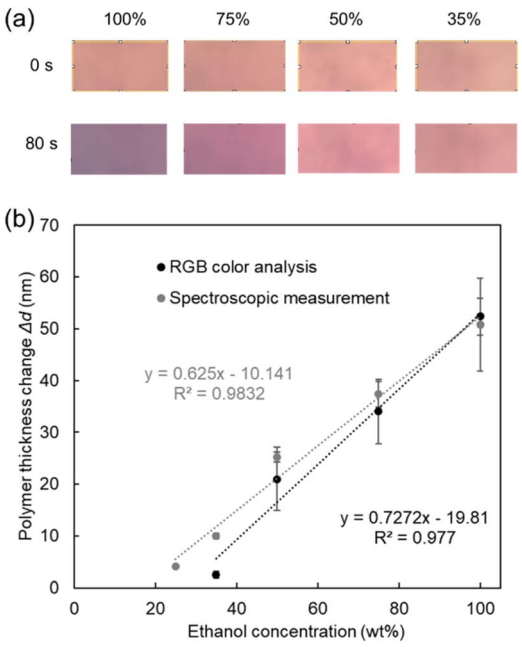

Fig. 7 From color to concentration. (a) Color photographs of the sensor surface when exposed to different concentrations of ethanol. (b) The correlation between ethanol concentration and the spacer thickness change at 80 s of ethanol exposure. The spacer thickness value is averaged from three repeat experiments for each ethanol concentration.

Conclusions

In summary, we present an optofluidic sensing platform consisting of a colorimetric sensor coupled to a micropillar array for efficient gas phase transfer of volatile analytes from liquid samples. The precise sample-sensor separation (enabled by the pillar array) offers a relatively large and homogeneous sensing region with close sample proximity, which will be stable in microgravity and can be detected by low resolution optics or by eye. The combination improves the sensing response time by an order of magnitude (minutes to seconds) and can be packaged in a compact format. This platform may be applied towards real-time human health monitoring—especially in low-resource settings (*e.g.*, long-duration human spaceflight)—where simplicity and ease of operation are important, along with accuracy and sensing performance.

Author contributions

Conceptualization: C. P., F. A. M., M. A. L. and T. J. P.; supervision, project administration, resources: C. P. and F. A. M.; investigation: T. J. P. and B. G.; methodology: T. J. P., B. G., B. H. B., M. A. L. and C. P.; formal analysis: T. J. P., B. G. and B. H. B.; writing – original draft: T. J. P. and B. G.; writing – review & editing: T. J. P., B. G., B. H. B., M. A. L., C. P. and F. A. M.

Notice for copyrighted information

Conflicts of interest

There are no conflicts to declare.

Acknowledgements

This collaboration was performed under an International Collaborative Umbrella Agreement between NASA and the Australian National Fabrication Facility (ANFF) (Agreement Number AS-0280-0), and was supported by the Australian Academy of Science Regional Collaborations Programme and the infrastructure at the South Australia Node of ANFF (ANFF-SA). The authors would like to thank Dr Gary W. Hunter (NASA Glenn Research Center) for helpful discussions and suggestions on the content of the manuscript. The authors also thank Dr Moein Kashani (University of South Australia) and Mr Zane Peterkovic (University of South Australia) for preliminary work not reported here.

References

1 A. E. Cetin, A. F. Coskun, B. C. Galarreta, M. Huang, D. Herman, A. Ozcan and H. Altug, *Light: Sci. Appl.*, 2014, **3**, e122.
2 M. Mesch, C. Zhang, P. V. Braun and H. Giessen, *ACS Photonics*, 2015, **2**, 475–480.
3 M. Sun, R. Bai, X. Yang, J. Song, M. Qin, Z. Suo and X. He, *Adv. Mater.*, 2018, **30**, 1804916.
4 A. Tadimety, Y. Zhang, K. M. Kready, T. J. Palinski, G. J. Tsongalis and J. X. J. Zhang, *Biosens. Bioelectron.*, 2019, **130**, 236–244.
5 J.-F. Masson, *Analyst*, 2020, **145**, 3776–3800.
6 A. Tadimety, Z. Wu, J. H. Molinski, R. Beckerman, C. Jin, L. Zhang, T. J. Palinski and J. X. J. Zhang, *Sci. Rep.*, 2021, **11**, 14185.
7 A. Roda, M. Mirasoli, M. Guardigli, M. Zangheri, C. Caliceti, D. Calabria and P. Simoni, *Biosens. Bioelectron.*, 2018, **111**, 18–26.
8 G. Chen, J. Zheng, L. Liu and L. Xu, *Small Methods*, 2019, **3**, 1900688.
9 S. Li, Z. Ma, Z. Cao, L. Pan and Y. Shi, *Small*, 2020, **16**, 1903822.
10 A. Bag and N.-E. Lee, *Adv. Mater. Technol.*, 2021, **6**, 2000883.
11 J. Kim, A. S. Campbell, B. E.-F. de Ávila and J. Wang, *Nat. Biotechnol.*, 2019, **37**, 389–406.
12 F. Khoshmanesh, P. Thurgood, E. Pirogova, S. Nahavandi and S. Baratchi, *Biosens. Bioelectron.*, 2021, **176**, 112946.
13 B. Lee, M. Lim and V. Misra, *2021 IEEE Sensors*, Sydney, Australia, 2021, DOI: **10.1109/SENSORS47087.2021.9639471**.
14 B. de Lacy Costello, A. Amann, H. Al-Kateb, C. Flynn, W. Filipiak, T. Khalid, D. Osborne and N. M. Ratcliffe, *J. Breath Res.*, 2014, **8**, 014001.
15 A. Amann, B. d. L. Costello, W. Miekisch, J. Schubert, B. Buszewski, J. Pleil, N. Ratcliffe and T. Risby, *J. Breath Res.*, 2014, **8**, 034001.
16 T. Issitt, L. Wiggins, M. Veysey, S. T. Sweeney, W. J. Brackenbury and K. Redeker, *J. Breath Res.*, 2022, **16**, 024001.
17 M. Phillips, R. Byrnes, R. N. Cataneo, A. Chaturvedi, P. D. Kaplan, M. Libardoni, V. Mehta, M. Mundada, U. Patel, N. Ramakrishna, P. B. Schiff and X. Zhang, *J. Breath Res.*, 2013, **7**, 036002.
18 M. Phillips, F. Grun and P. Schmitt, *J. Breath Res.*, 2022, **16**, 026002.
19 X. Fan and I. M. White, *Nat. Photonics*, 2011, **5**, 591.
20 L. Pang, H. M. Chen, L. M. Freeman and Y. Fainman, *Lab Chip*, 2012, **12**, 3543–3551.
21 J. Wu, B. Dai, Z. Li, T. Pan, D. Zhang and F. Lin, *VIEW*, 2021, **2**, 20200035.
22 F. Liu, B. Q. Dong, X. H. Liu, Y. M. Zheng and J. Zi, *Opt. Express*, 2009, **17**, 16183–16191.
23 M. Qin, M. Sun, R. Bai, Y. Mao, X. Qian, D. Sikka, Y. Zhao, H. J. Qi, Z. Suo and X. He, *Adv. Mater.*, 2018, **30**, 1800468.
24 Z. Xuan, J. Li, Q. Liu, F. Yi, S. Wang and W. Lu, *The Innovation*, 2021, **2**, 100081.
25 T. J. Palinski, A. Tadimety, I. Trase, B. E. Vyhnalek, G. W. Hunter, E. Garmire and J. X. J. Zhang, *Opt. Express*, 2021, **29**, 25000–25010.
26 J. Xue, Z.-K. Zhou, Z. Wei, R. Su, J. Lai, J. Li, C. Li, T. Zhang and X.-H. Wang, *Nat. Commun.*, 2015, **6**, 8906.
27 Z. Yang, C. Ji, D. Liu and L. J. Guo, *Adv. Opt. Mater.*, 2019, **7**, 1900739.
28 Y. Dong, E. M. Akinoglu, H. Zhang, F. Maasoumi, J. Zhou and P. Mulvaney, *Adv. Funct. Mater.*, 2019, **29**, 1904290.
29 J. Jang, K. Kang, N. Raeis-Hosseini, A. Ismukhanova, H. Jeong, C. Jung, B. Kim, J.-Y. Lee, I. Park and J. Rho, *Adv. Opt. Mater.*, 2020, **8**, 1901932.
30 C. Semprebon, P. Forsberg, C. Priest and M. Brinkmann, *Soft Matter*, 2014, **10**, 5739–5748.
31 M. K. Orlowska, B. Guan, R. Sedev, Y. Morikawa, K. Suu and C. Priest, *Anal. Chem.*, 2020, **92**, 16043–16050.
32 G. Holzner, F. H. Kriel and C. Priest, *Anal. Chem.*, 2015, **87**, 4757–4764.
33 D. Ambrose and C. H. S. Sprake, *J. Chem. Thermodyn.*, 1970, **2**, 631–645.
34 J. Junesch, T. Sannomiya and A. B. Dahlin, *ACS Nano*, 2012, **6**, 10405–10415.
35 P. B. Johnson and R. W. Christy, *Phys. Rev. B: Solid State*, 1972, **6**, 4370–4379.
36 J. S. Papanu, D. W. Hess, D. S. Soane and A. T. Bell, *J. Appl. Polym. Sci.*, 1990, **39**, 803–823.
37 J. Lv, D. Chen, Y. Du, T. Wang, X. Zhang, Y. Li, L. Zhang, Y. Wang, R. Jordan and Y. Fu, *ACS Sensors*, 2020, **5**, 303–307.
38 I. Tokareva, I. Tokarev, S. Minko, E. Hutter and J. H. Fendler, *Chem. Commun.*, 2006, 3343–3345, DOI: **10.1039/B604841B**.
39 N. Sharma, C. Petri, U. Jonas, M. Bach, G. Tovar, K. Mrkvová, M. Vala, J. Homola, W. Knoll and J. Dostálek, *Macromol. Chem. Phys.*, 2014, **215**, 2295–2304.

40 P. Lova, C. Bastianini, P. Giusto, M. Patrini, P. Rizzo, G. Guerra, M. Iodice, C. Soci and D. Comoretto, *ACS Appl. Mater. Interfaces*, 2016, **8**, 31941–31950.
41 D.-H. Park, J.-M. Heo, W. Jeong, Y. H. Yoo, B. J. Park and J.-M. Kim, *ACS Appl. Mater. Interfaces*, 2018, **10**, 5014–5021.
42 H. Lin, M. Jang and K. S. Suslick, *J. Am. Chem. Soc.*, 2011, **133**, 16786–16789.
43 A. T. Sanda Mahama, A. S. Dossa and P. Gouton, *Electronic Imaging*, 2016, 1–4.
44 Y. Hou and R. E. Baltus, *Ind. Eng. Chem. Res.*, 2007, **46**, 8166–8175.
45 G. I. Sarser and N. G. Kalinin, *Mater. Sci.*, 1975, **9**, 610–611.